

Article

Thermal Stability of CsPbBr₃ Perovskite Quantum Dots Assembled with SBA-15

Hongyu Chen ¹, Yunfei Wang ¹, Jianing Wang ² and Wenyan Liu ^{1,3,*}

¹ Department of Physics, School of Sciences, Beihua University, Jilin 132013, China; hyuchen0309@163.com (H.C.); w211616@126.com (Y.W.)

² Changchun Institute of Optics, Fine Mechanics and Physics, Chinese Academy of Sciences, Changchun 130033, China; qazedcfv@sina.com

³ Department of Materials Science and Engineering, Beihua University, Jilin 132013, China

* Correspondence: wylu1234@163.com; Tel.: +86-186-0449-5978

Abstract: Nowadays, the excellent performance of metal halide perovskite quantum dots (PQDs) has been demonstrated, but the stability is still a perplexing issue. In this paper, the CsPbBr₃ QDs were assembled into SBA-15 for the first time. The thermal stability and photoluminescence (PL) intensity of SBA-15@CsPbBr₃ QDs were improved. The PL spectra of pure CsPbBr₃ QDs have red-shift (~6 nm) with the increasing temperature. However, that of SBA-15@CsPbBr₃ QDs have almost no red-shift. The PL intensity of SBA-15@CsPbBr₃ QDs decreased slightly after heating and cooling for several times. By comparison, the PL intensity of pure CsPbBr₃ QDs decreased more significantly. The experimental results showed that SBA-15 played a significant role in improving the thermal stability of PQDs, which will have an excellent potential for the application of PQDs in the future.

Keywords: CsPbBr₃ QDs; SBA-15; thermal stability



Citation: Chen, H.; Wang, Y.; Wang, J.; Liu, W. Thermal Stability of CsPbBr₃ Perovskite Quantum Dots Assembled with SBA-15. *Coatings* **2021**, *11*, 953. <https://doi.org/10.3390/coatings11080953>

Academic Editor: Xiaoyu Zhang

Received: 17 July 2021

Accepted: 6 August 2021

Published: 9 August 2021

Publisher's Note: MDPI stays neutral with regard to jurisdictional claims in published maps and institutional affiliations.



Copyright: © 2021 by the authors. Licensee MDPI, Basel, Switzerland. This article is an open access article distributed under the terms and conditions of the Creative Commons Attribution (CC BY) license (<https://creativecommons.org/licenses/by/4.0/>).

1. Introduction

Recently, the global demand for lighting, display and other fields has increased sharply [1]. It has been found that semiconductor light-emitting diodes (LED) are more energy efficient than traditional lighting display devices [2–4]. However, LED devices made from conventional inorganic semiconductor materials need to strictly control the preparation conditions, and their production and efficiency are limited by high production costs and high ohmic contact resistance [5–7]. Organic light-emitting diodes (OLED), by contrast, greatly improve the relevant performance, but their efficiency will be reduced at high current densities [8]. Therefore, perovskite has been widely concerned in the field of optoelectronics due to its advantages of tunable band gap, high light absorption coefficient, small exciton binding energy and high charge mobility. It is generally believed that perovskite materials an ideal direct band gap semiconductor as raw material for light-emitting devices [9]. Metal halide perovskites (MHPs) have become a new generation of light-emitting materials due to their fantastic optoelectronic properties, such as high color purity, tunable band gaps, bipolar conduction, etc. [10].

Semiconductor quantum dots (QDs) are becoming the focus of research due to their unique properties [8,11–13]. Quantum limiting effect is the most significant characteristic of QDs [14,15]. The three-dimensional (3D) quantum limiting effect of carriers in quantum dots is caused by low density of state and high energy level sharpness, which also changes the electrical and optical properties of quantum dots [16]. Semiconductor QDs have an excellent promise for wide application such as in single electronic devices, memory devices and various optoelectronic devices due to the properties above [17].

Metal halide perovskite quantum dots are zero-dimensional nano materials, which have tunable emission spectrum, high light stability and long fluorescence lifetime due to quantum limiting effect [18]. Especially, lead halide perovskite nanocrystals are suitable for

solid-state lighting and high-definition display applications due to their wide color gamut (NTSC \approx 140%) [19,20], high color purity [21], as well as facile synthesis methods [22–25]. The external quantum efficiency (EQE) of LEDs based on perovskite quantum dots mainly depends on the quality of the luminescent layer, and the quality can be improved by optimizing the preparation method and adjusting the composition [26–30]. Compared with 2D and 3D perovskite, the perovskite quantum dot films have many advantages, such as high color gamut, pure color, stable performance and so on. Therefore, the photovoltaic devices based on the perovskite quantum dot films will have better performance [31]. However, the thermal stability of PQDs has been restricting their development [32].

There are many factors which are affecting the thermal stability of PQDs, the most important is the uneven grain size distribution [33], which leads to the increase of defects in the crystal. During the continuous heating process, the internal stress inhomogeneity of PQD lattice begins to produce, which makes the lattice distorted until the perovskite structure begins to collapse [34]. Therefore, we believe that the fundamental way to solve this problem is to adopt a new method to synthesize quantum dots [35–37], so that their grain distribution is more uniform with good dispersion. Template synthesis is one of the feasible methods at present, which is using mesoporous materials as template to make the synthesized PQDs' grains have better dispersion, thus reducing the internal defects of the crystal lattice, greatly reducing the internal stress of the crystal lattice and improving the thermal stability [38,39].

SBA series mesoporous silicon materials are named from the University of California, Santa Barbara, which is the abbreviation of Santa Barbara amorphous [40]. Among them, SBA-15 is more famous. SBA-15 is a mesoporous silica with a fine pore diameter arrangement and controllable pore diameter between 5 to 15 nm [41]. SBA-15 compared with older mesoporous silica has larger pores and thicker walls (3.1–6.4 nm), these make SBA-15 yields with good thermal, mechanical stability and chemical resistance properties [42]. The structure of SBA-15 is an ordered hexagonal and it was also synthesized using triblock copolymer. The surface area of neat SBA-15 could be up to 650 m²/gr [43,44].

In this paper, we synthesized the PQDs by ligand assisted precipitation (LAPR) method at room temperature and using SBA-15 as a template. By using SBA-15 as a template, the growth of PQDs during the preparation process was strictly controlled to make its crystallization more uniform, thus improving the thermal stability and the intensity of PL spectra of PQDs.

2. Materials and Methods

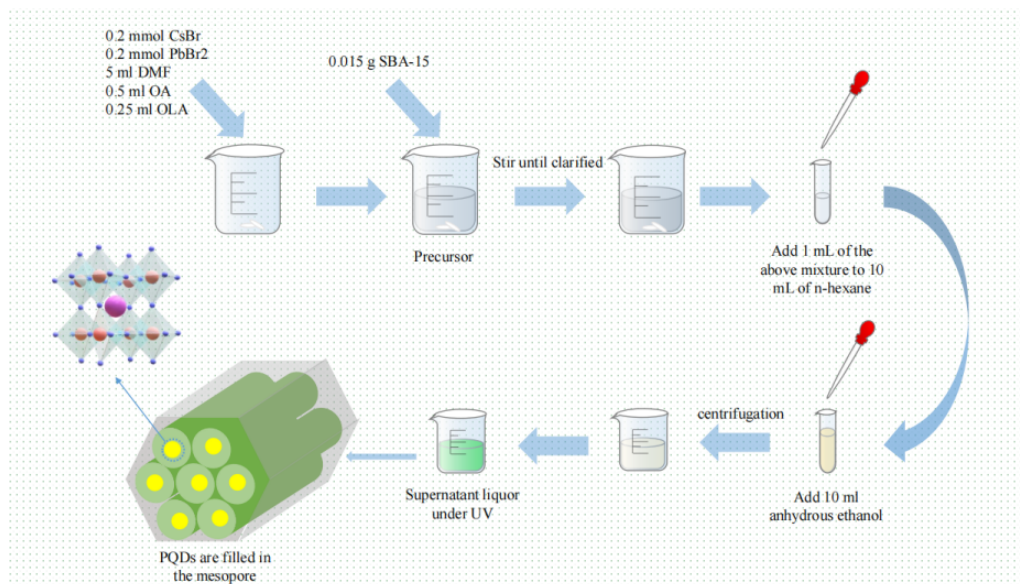
2.1. Experimental Materials

Cesium bromide (CsBr, 99.9%, Aladdin Industrial Corporation, Shanghai, China), lead (II) bromide (PbBr₂, 99.0%, Aladdin Industrial Corporation, Shanghai, China), oleic acid (OA, 90%, Aladdin Industrial Corporation, Shanghai, China), oleylamine (OLA, 90%, from Aladdin Industrial Corporation, Shanghai, China), N,N-dimethylformamide (DMF, 99.9%, Sigma-Aldrich, Shanghai, China), hexane (99%, Aladdin Industrial Corporation, Shanghai, China), ethyl alcohol (99.7%, Aladdin Industrial Corporation, Shanghai, China), 1-octadecene (ODE, 99.5%, Aladdin Industrial Corporation, Shanghai, China) SBA-15 (6–11nm, Jiangsu XFNANO Materials Tech, Nanjing, China), KnNa_{12-n}((AlO₂)₁₂(SiO₂)₁₂)·xH₂O (molecular sieves, 3 Å, Aladdin Industrial Corporation, Shanghai, China). DMF (Sigma-Aldrich, Shanghai, China), hexane (Aladdin Industrial Corporation, Shanghai, China), ODE (Aladdin Industrial Corporation, Shanghai, China) and ethyl alcohol (Sigma-Aldrich, Shanghai, China) are added to K_nNa_{12-n}((AlO₂)₁₂(SiO₂)₁₂)·xH₂O.

2.2. Synthesis of CsPbBr₃ QDs

As shown in Scheme 1, perovskite nanocrystals were synthesized by LAPR method at room temperature; 0.043 g (0.2 mmol) CsBr and 0.073 g (0.2 mmol) PbBr₂ were dissolved in DMF (5 mL), OA (0.5 mL) and OLA (0.25 mL), and the precursor solution was obtained. The precursor solution was stirred until all the solids were dissolved and a clear solution was

obtained; 1 mL of the precursor mixture was injected into 10 mL of hexane in a centrifuge tube, adding 10 mL of anhydrous ethanol and centrifuged at 6000 rpm for 6 min. Finally, the supernatant was dumped and the CsPbBr₃ QDs was collected for further characterization.



Scheme 1. Schematic illustration of formation of SBA-15@CsPbBr₃ QDs.

2.3. Synthesis of SBA-15@CsPbBr₃ QDs

Solutions containing SBA-15@CsPbBr₃ QDs were prepared using the method described in Section 2.2. Then, 0.015 g of SBA-15 was added to the precursor and the mixture was stirred until all the solids were dissolved completely. Following, 1 mL of the mixture was injected into 10 mL of hexane. The products were centrifuged at 6000 rpm for 12 min. Finally, the supernatant was dumped and the SBA-15@CsPbBr₃ QDs was collected for further characterization.

2.4. Characterizations

The X-ray diffraction (XRD) patterns of the CsPbBr₃ QDs and SBA-15@CsPbBr₃ QDs were measured by a Cu K α radiation using XRD-6100 (X'Pert PRO, PANalytical, Amsterdam, The Netherlands). Fourier Transform Infrared (FTIR) spectra were performed using KBr tablets and a Nicolet iS50 FT-IR Spectrometer (Thermo Fisher Scientific, Waltham, MA, USA). The transmission electron microscope (TEM) images were recorded by a transmission electron microscope (JEM 2100F, JEOL, Tokyo, Japan). For the characterization of TEM, the samples were formed film on the ultra-thin carbon film. The Energy Dispersive Spectrometer (EDS) spectra were measured by scanning electron microscope (SEM), (UHR FE-SEM SU8000, Hitachi High-Technologies, Tokyo, Japan). Absorption spectra were measured by a UV-Vis spectrophotometer (UV-2700, Bruker, Karlsruhe, Germany). The samples were dissolved in hexane. Photoluminescence (PL) spectra were measured by a fluorescence spectrophotometer (Omni PL-BH, Zolix, Beijing, China), a 405 nm laser was used as the excitation source. All tests above were done at room temperature. For temperature-dependent PL spectra, the samples were dissolved in 1-octadecene.

3. Results and Discussion

The absorption and PL spectra of CsPbBr₃ QDs and SBA-15@CsPbBr₃ QDs were shown in Figure 1. As shown in Figure 1a, the absorption peaks of CsPbBr₃ QDs and SBA-15@CsPbBr₃ QDs were 498 nm and 515 nm, respectively. The red-shift of the absorption peaks was due to the adsorption of QDs on the surface of SBA-15 and the formation of slightly bigger particles. The PL spectra of CsPbBr₃ QDs and SBA-15@CsPbBr₃ QDs at the same concentration was shown in Figure 1b. At the excitation wavelength of 405 nm,

the PL intensity of CsPbBr₃ QDs was slightly lower than SBA-15@CsPbBr₃ QDs, and the latter produced a slight red-shift. The emission wavelength of pure CsPbBr₃ QDs and SBA-15@CsPbBr₃ QDs were 515 nm and 519 nm, respectively. A red-shift of 4 nm occurred; this might be due to the increased size of SBA-15 when it was assembled with CsPbBr₃ QDs. Additionally, their narrow full width at half maxima (FWHM) were around 22 nm and 23 nm, respectively. There was no significant change in FWHM due to the introduction of SBA-15. The photoluminescence quantum yield (PLQY) of CsPbBr₃ QDs was 50% and that of SBA-15@CsPbBr₃ QDs was 60%. The PLQY and temperature dependence PLQY have been measured. The PLQY of the two samples at different temperatures was compared. The quantum efficiency with different temperatures have been measured. The PLQY of CsPbBr₃ QDs remained ~7% of initial PLQY at 70 °C. In contrast, the PLQY of SBA-15@CsPbBr₃ remained ~21% of initial PLQY at 70 °C. The mesoporous of SBA-15 are open channel. Therefore, the air and water also can influence the PL intensity of SBA-15@CsPbBr₃ QDs. However, as a template, SBA-15 can inhibit the agglomeration of quantum dots during heating, which can be proved from the fact that the position of PL peak hardly changes with the increasing temperature.

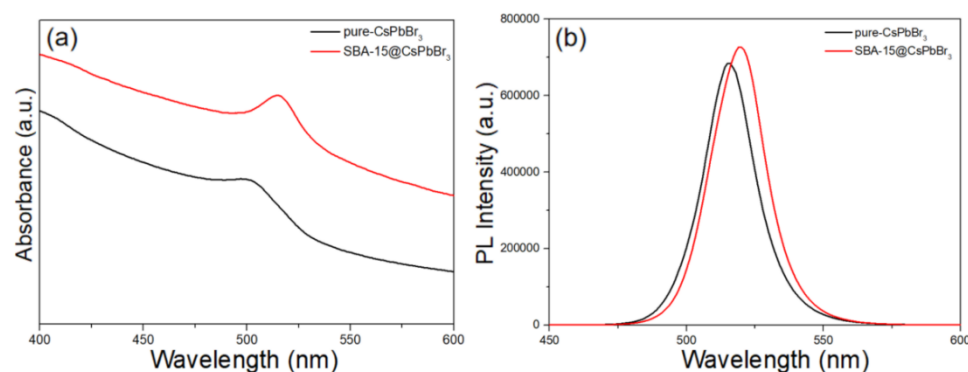


Figure 1. (a) UV-Vis absorption of pure CsPbBr₃ QDs (black) and SBA-15@CsPbBr₃ QDs (red); (b) PL spectra of pure CsPbBr₃ QDs (black) and SBA-15@CsPbBr₃ QDs (red).

The TEM photographs were shown in Figure 2a,b, which indicate the particle sizes of CsPbBr₃ QDs and SBA-15@CsPbBr₃ QDs which were 3 and 6 nm, respectively. The size and distribution of CsPbBr₃ QDs and SBA-15@CsPbBr₃ QDs were shown in Figure 2c,d. In Figure 3, the energy-dispersive spectroscopy (EDS) elemental mapping of the CsPbBr₃ QDs and SBA-15@CsPbBr₃ QDs films are shown. As shown in Figure 3i,j, from which a distribution of Si elements in the selected square area was clearly seen, the EDS peak of Si has been observed in SBA-15@CsPbBr₃ QDs. The mole fraction of each element in CsPbBr₃ QDs and SBA-15@CsPbBr₃ QDs was shown in Table 1. The mole fraction of Si was 0 in CsPbBr₃ QDs and 30.7 in SBA-15@CsPbBr₃ QDs.

For further research, FTIR spectra of pure CsPbBr₃ QDs and SBA-15@CsPbBr₃ QDs were measured, as shown in Figure 4. The peaks at around 3414 and 1626 cm⁻¹ were found in the FTIR spectra of pure CsPbBr₃ QDs and SBA-15@CsPbBr₃ QDs, and there were the symmetric stretching of N–H bond and the asymmetric of NH⁺, respectively. The peaks at 2853 cm⁻¹/2857 cm⁻¹ and 2923 cm⁻¹/2927 cm⁻¹ were attributed to C–H tensile vibrations of the ligands of pure CsPbBr₃ QDs and SBA-15@CsPbBr₃ QDs. For the red curve in Figure 4, there were two obvious peaks at 797 and 1095 cm⁻¹, which correspond to the symmetric and anti-symmetric tensile vibration modes of the Si–O–Si group of SBA-15@CsPbBr₃ QDs. A peak of 1390 cm⁻¹ was corresponded to CH₃ vibration mode. The peaks of 968 cm⁻¹ and 1651 cm⁻¹ were related to vibration of Si–OH and H–OH group. The existence of H–OH bond indicated that the CsPbBr₃ QDs were dispersed in the mesoporous channels of SBA-15.

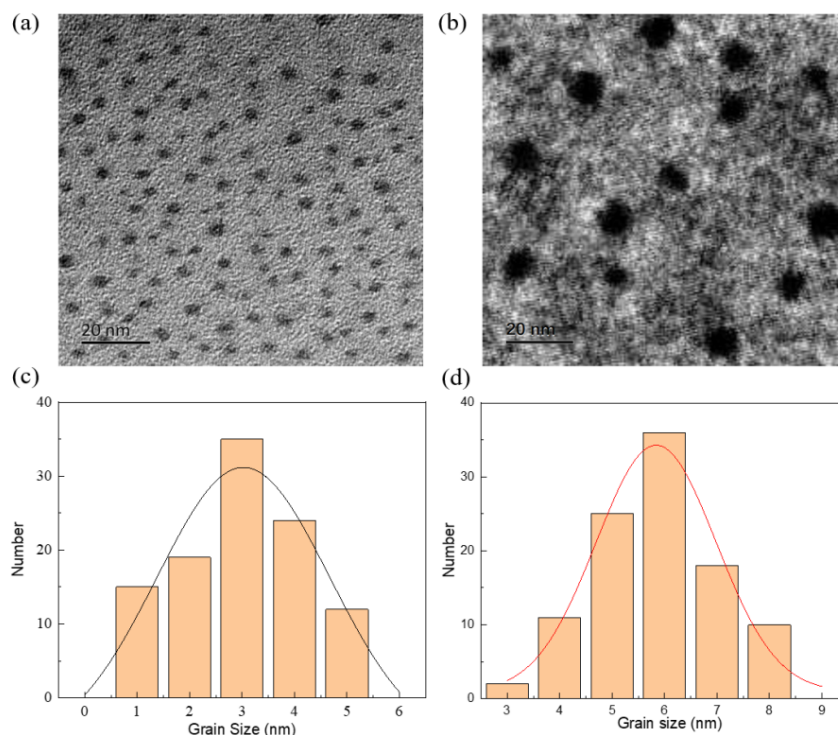


Figure 2. TEM images and distribution of grain size of pure CsPbBr₃ QDs (a,c) and SBA-15@CsPbBr₃ QDs (b,d).

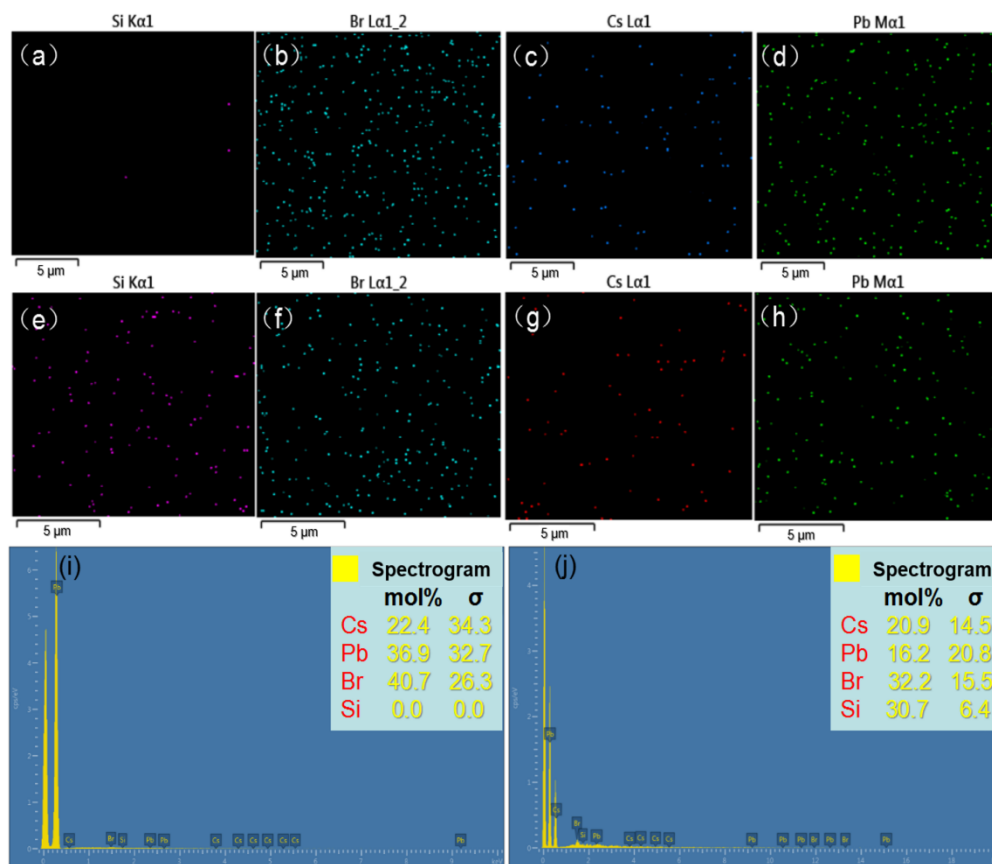
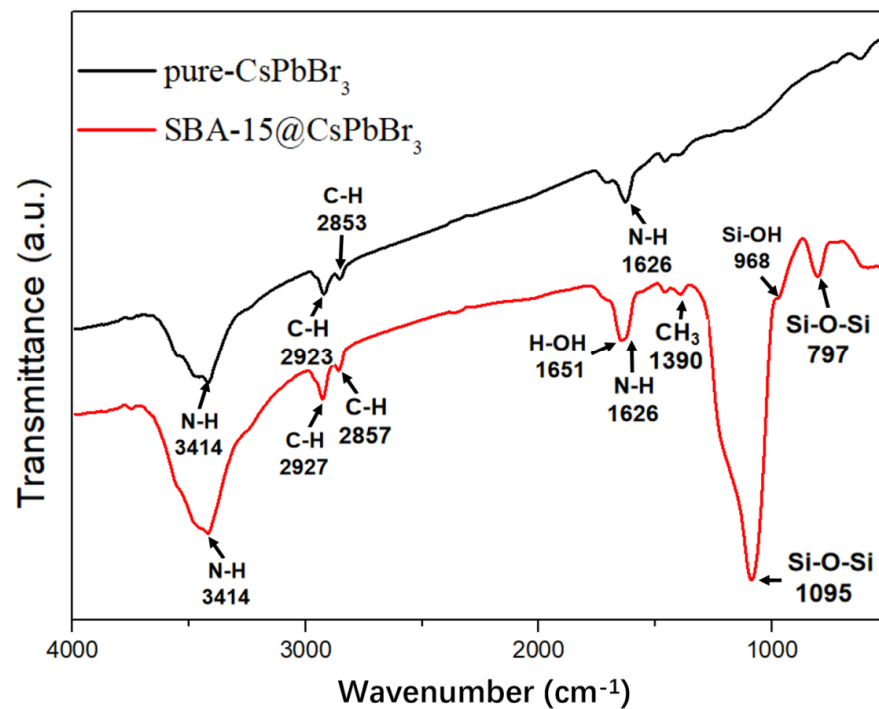


Figure 3. The EDS images of CsPbBr₃ QDs (a–d) and SBA-15@CsPbBr₃ QDs (e–h). The elemental proportion of CsPbBr₃ QDs (i) and SBA-15@CsPbBr₃ QDs (j).

Table 1. The elemental mole fraction of CsPbBr₃ QDs and SBA-15@CsPbBr₃ QDs.

Atoms	CsPbBr ₃ (mol%)	SBA-15@CsPbBr ₃ (mol%)
Cs	22.4	20.9
Pb	36.9	16.2
Br	40.7	32.2
Si	0	30.7

**Figure 4.** FTIR of (black) CsPbBr₃ QDs and (red) SBA-15@CsPbBr₃ QDs.

The XRD images of pure CsPbBr₃ QDs and SBA-15@CsPbBr₃ QDs were shown in Figure 5. The black curve of pure CsPbBr₃ QDs showed strong diffraction peaks at 15.19°, 21.55°, 30.65°, 34.37°, 37.77° and 43.89°, corresponding to cubic CsPbBr₃ (PDF#00-054-0752) (100), (110), (200), (210), (211) and (220) planes, respectively. Comparing to the two XRD curves, it was found that all the characteristic peaks of pure CsPbBr₃ QDs could be found in the curve of SBA-15@CsPbBr₃ QDs, which indicated that the structure of pure CsPbBr₃ QDs was preserved without destruction after assembling into SBA-15.

Figure 6 showed the temperature-dependent PL spectra of pure CsPbBr₃ QDs and SBA-15@CsPbBr₃ QDs at room temperature—100 °C under the same environment conditions. The PL spectra of SBA-15@CsPbBr₃ QDs decreased less than that of CsPbBr₃ QDs with increasing temperature, especially at lower temperature, although the PL intensity of both materials decreased significantly. The peak position of pure CsPbBr₃ QDs moved from 515 nm (RT) to 521 nm with the increasing temperature. Nevertheless, the peak position of SBA-15@CsPbBr₃ QDs was 519 nm and there was almost no red-shift in the peak position. The data above proved that the thermal stability of SBA-15@CsPbBr₃ QDs was better than that of pure CsPbBr₃ QDs.

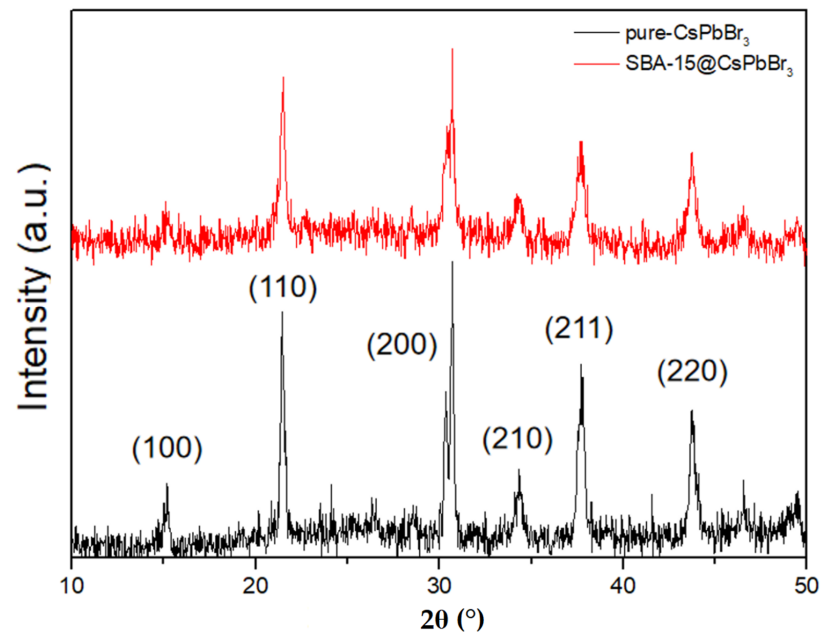


Figure 5. XRD pattern of pure CsPbBr₃ QDs (black) and SBA-15@CsPbBr₃ QDs (red).

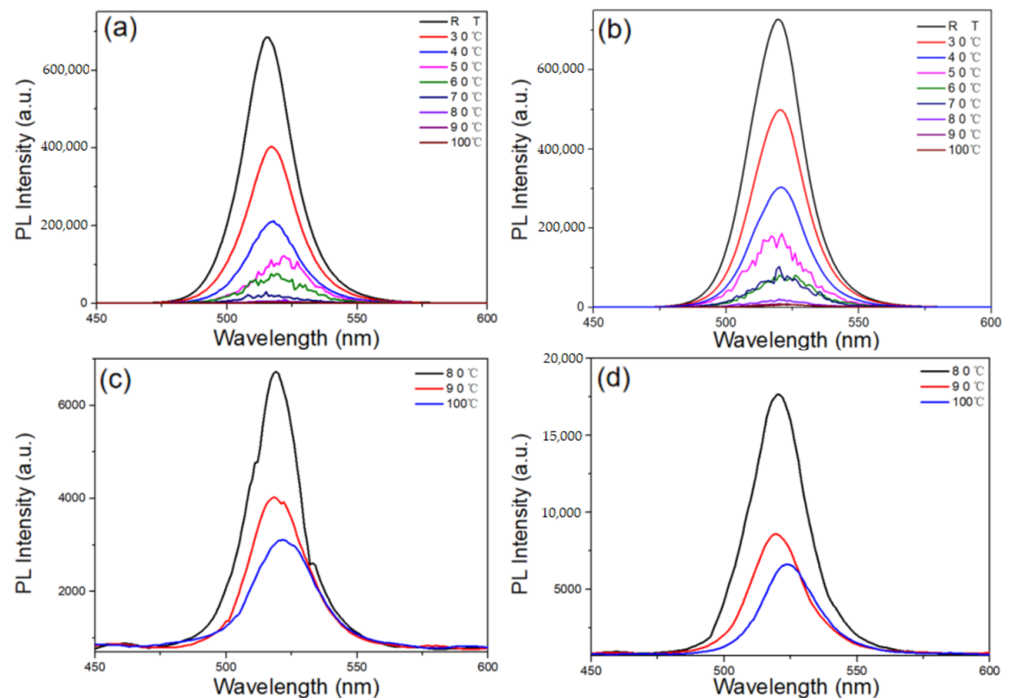


Figure 6. PL spectra of (a) pure CsPbBr₃ QDs and (b) SBA-15@CsPbBr₃ QDs from room temperature to 100 °C; PL spectra of (c) pure CsPbBr₃ QDs and (d) SBA-15 CsPbBr₃ QDs at 80, 90, and 100 °C.

The PL spectra of the pure CsPbBr₃ QDs and SBA-15@CsPbBr₃ QDs with the number of cycles were shown in Figure 7. The PL spectrum was measured after PQDs was raised to 100 °C and cooled to room temperature. As shown in Figure 7a, the PL intensity of pure CsPbBr₃ QDs falling back to room temperature after the second rise to 100 °C was about a quarter of that of the first. In addition, the PL intensity decreased significantly after each heating and cooling cycle, and the luminescence was very weak which was shown in Figure 7c. By contrast, the PL intensity of SBA-15@CsPbBr₃ QDs was a third of the first after two times of heating to 100 °C and cooling to room temperature which was shown in Figure 7b. The PL intensity of CsPbBr₃ QDs and SBA-15@CsPbBr₃ QDs

decreased significantly mainly due to the falling of ligands (OA or OLA) from the surface of QDs and the additional structural defects caused by the first thermal cycle. Therefore, the PL intensity after first thermal cycle decreased more significantly than that of second, third and fourth time thermal cycle. Compared with CsPbBr₃ QDs, the PL intensity of the SBA-15@CsPbBr₃ QDs experienced a relatively slower decrease after second, third and fourth time thermal cycle. The mesoporous of SBA-15 are open channel. Therefore, the air and water also can influence the PL intensity of SBA-15@CsPbBr₃ QDs. However, as a template, SBA-15 can inhibit the agglomeration of quantum dots during heating, which can be proved from the fact that the position of PL peak hardly changes with the increasing temperature.

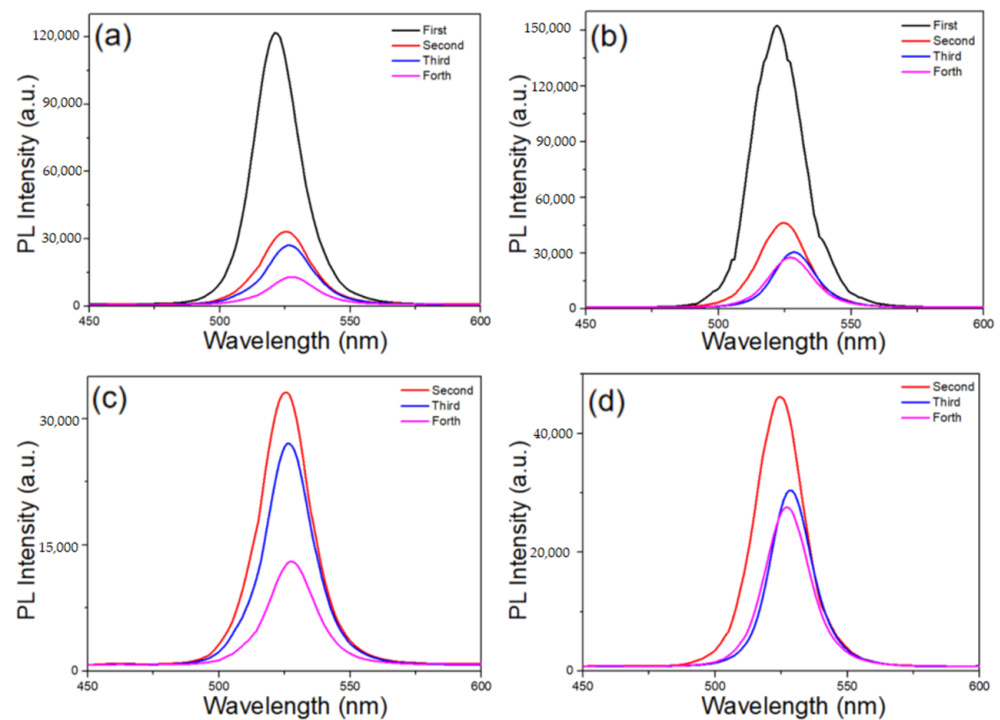


Figure 7. The PL spectra of (a) pure CsPbBr₃ QDs and (b) SBA-15 CsPbBr₃ QDs after heating and cooling cycle. The PL spectra of (c) pure CsPbBr₃ QDs and (d) SBA-15@CsPbBr₃ QDs' heating and cooling cycle for the last three times.

As shown in Figure 8, it was found that all the characteristic peaks of pure CsPbBr₃ QDs and SBA-15@CsPbBr₃ QDs could be found after heating and cooling cycle, which indicated that the structure of pure CsPbBr₃ QDs and SBA-15@CsPbBr₃ QDs was preserved without destruction. The PL intensity of pure CsPbBr₃ QDs decreased significantly mainly due to the falling of ligands (OA or OLA) from the surface of QDs and the additional structural defects caused by the heating. In contrast, the PL intensity of the SBA-15@CsPbBr₃ QDs experienced a relatively slower decrease.

The liquid-type fluorescent LED based on SBA-15@CsPbBr₃ QDs has been fabricated as shown in Figure 9. For the typical fabrication process of LED devices as follows: two large pieces of glass (the size is 1.7 cm × 1.7 cm with the thickness of 0.1 cm) and four thin stripes (two of them: 1.7 cm × 0.3 cm and the other: 1 cm × 0.3 cm) were cut and then cleaned by deionized water and ethanol. These four thin stripes were sandwiched between two large pieces of glass, and a liquid-type glass tank with the size of 1 cm × 1 cm was left. In addition, the two gaps with the width of 0.1 cm were left in order to make the air get out of the glass box when liquid-type QDs were loaded. Then the glass box was filled with QD solution and sealed all the gaps with epoxy-based glue. Finally, monochromatic QD-LEDs were fabricated by integrating the sealed glass box with UV LED chip (emission peak at 365 nm).

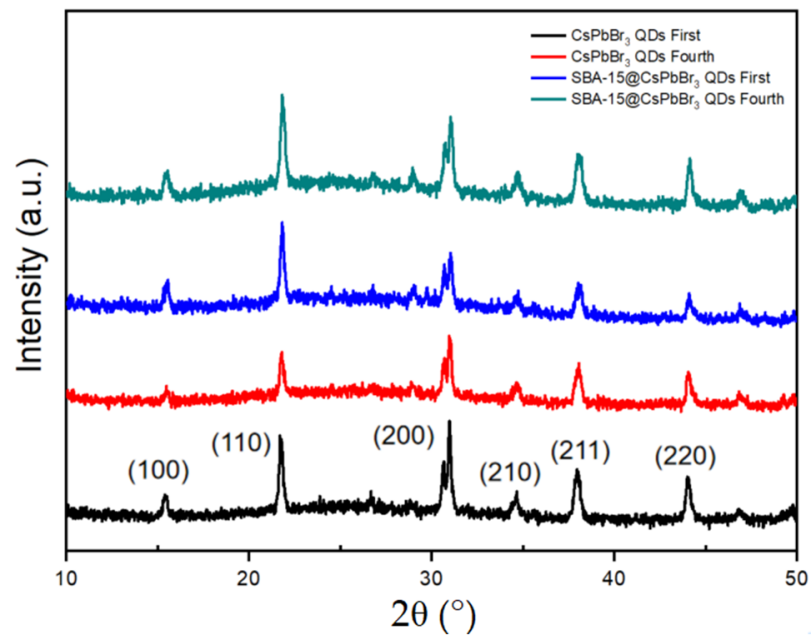


Figure 8. XRD pattern of pure CsPbBr₃ QDs and SBA-15@CsPbBr₃ QDs after heating and cooling.

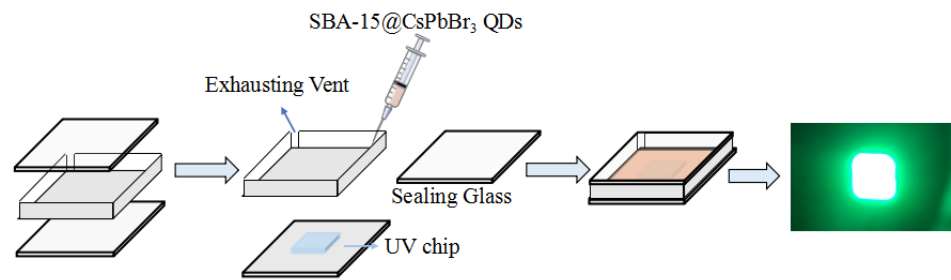


Figure 9. The process flow of liquid-type QD-LEDs and the picture of LED sample with green emission color operated at 3.2 V under a dark condition.

The luminance of the LED is shown in Figure 10 which was worked on 2.6 V, 2.8 V, 3.0 V and 3.2 V.

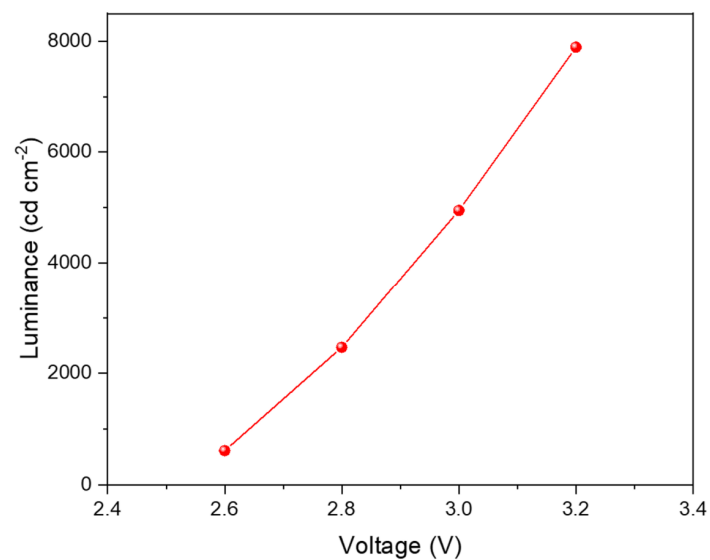


Figure 10. The luminance of SBA-15@CsPbBr₃ QD-LED at different voltage.

4. Conclusions

In summary, by using SBA-15 as the template, the growth of CsPbBr₃ QDs is controlled in this paper, and the stability of the PQDs is improved by uniform crystallization. Compared with pure CsPbBr₃ QDs, the thermal stability of SBA-15@CsPbBr₃ QDs was better. In the heating experiment, the PL intensity of pure CsPbBr₃ QDs decreased rapidly and greatly. However, that of SBA-15@CsPbBr₃ QDs decreased more slightly, especially at high temperature. The PL spectra of pure CsPbBr₃ QDs has red-shift (~6 nm) with the increasing temperature, but did not occur at that of SBA-15@CsPbBr₃ QDs. In addition, the PL intensity of SBA-15@CsPbBr₃ QDs decreased less than that of CsPbBr₃ QDs significantly after four times of heating and cooling. The results showed that this method can solve the problem of improving the thermal stability of perovskite, which shows a broad prospect in the stability of perovskite. Although the results given in this paper are not perfect, it can provide a new research idea of PQDs based on SBA-15, which will make a significant contribution to improving the stability and practical application of these kinds of materials in the future.

Author Contributions: Data curation, H.C.; writing—original draft preparation, H.C.; investigation, Y.W.; literature search, Y.W.; principal analysis, J.W. interpretation data, J.W.; administration, W.L.; formulation of overarching research goals, W.L. All authors have read and agreed to the published version of the manuscript.

Funding: This research was funded by the National Natural Science Foundation of China, Grant Nos 61604003 and 62005268.

Institutional Review Board Statement: Not applicable.

Informed Consent Statement: Not applicable.

Data Availability Statement: Data sharing is not applicable to this article.

Conflicts of Interest: The authors declare that they have no known competing financial interests or personal relationships that could have appeared to influence the work reported in this paper.

References

1. Sun, S.; Yuan, D.; Xu, Y.; Wang, A.; Deng, Z. Ligand-mediated synthesis of shape-controlled cesium lead halide perovskite nanocrystals via reprecipitation process at room temperature. *ACS Nano* **2016**, *10*, 3648–3657. [[CrossRef](#)]
2. Lin, C.C.; Meijerink, A.; Liu, R.-S. Critical red components for next-generation white LEDs. *J. Phys. Chem. Lett.* **2016**, *7*, 495–503. [[CrossRef](#)] [[PubMed](#)]
3. Li, J.; Xu, L.; Wang, T.; Song, J.; Chen, J.; Xue, J.; Dong, Y.; Cai, B.; Shan, Q.; Han, B.; et al. 50-Fold EQE improvement up to 6.27% of solution-processed all-inorganic perovskite CsPbBr₃ QLEDs via surface ligand density control. *Adv. Mater.* **2017**, *29*, 1603885–1603894. [[CrossRef](#)] [[PubMed](#)]
4. Yuan, F.; Yuan, T.; Sui, L.; Wang, Z.; Xiaohong, L.; Li, Y.; Li, X.; Fanglong, Y.; Tan, Z.; Chen, A.; et al. Engineering triangular carbon quantum dots with unprecedented narrow bandwidth emission for multicolored LEDs. *Nat. Commun.* **2018**, *9*, 1–11. [[CrossRef](#)] [[PubMed](#)]
5. Wang, L.; Liu, H.; Zhao, J.; Zhang, X.; Zhang, C.; Zhang, G.; Liu, Q.; Duan, H. Enhancement of charge transport in porous carbon nanofiber networks via ZIF-8-enabled welding for flexible supercapacitors. *Chem. Eng. J.* **2020**, *382*, 122979–123012. [[CrossRef](#)]
6. Luyen, D.T.L.; Thanh, T.D.; Chuong, N.D.; Tuan, L.H.; Hoon, K.N.; Hee, L.J. Hierarchical three-dimensional framework interface assembled from oxygen-doped cobalt phosphide layer-shelled metal nanowires for efficient electrocatalytic water splitting. *Appl. Catal.* **2020**, *261*, 118268–118281. [[CrossRef](#)]
7. Septiani, N.L.W.; Kaneti, Y.V.; Fathoni, K.B.; Wang, J.; Ide, Y.; Yulianto, B.; Nugraha; Dipojono, H.K.; Nanjundan, A.K.; Golberg, D.; et al. Self-assembly of nickel phosphate-based nanotubes into two-dimensional crumpled sheet-like architectures for high-performance asymmetric supercapacitors. *Nano Energy* **2020**, *67*, 104270. [[CrossRef](#)]
8. Song, J.; Li, J.; Li, X.; Xu, L.; Dong, Y.; Zeng, H. Quantum dot light-emitting diodes based on inorganic perovskite cesium lead halides (CsPbX₃). *Adv. Mater.* **2015**, *27*, 7162–7167. [[CrossRef](#)]
9. Gul, I.; Sayed, M.; Shah, N.S.; Khan, J.A.; Polychronopoulou, K.; Iqbal, J.; Rehman, F. Solar light responsive bismuth doped titania with Ti³⁺ for efficient photocatalytic degradation of flumequine: Synergistic role of peroxy monosulfate. *Chem. Eng. J.* **2020**, *384*, 123255–123273. [[CrossRef](#)]
10. Chu, S.; Chen, W.; Fang, Z.; Xiao, X.; Liu, Y.; Chen, J.; Huang, J.; Xiao, Z. Large-area and efficient perovskite light-emitting diodes via low-temperature blade-coating. *Nat. Commun.* **2021**, *12*, 1–9. [[CrossRef](#)]

11. Im, J.-H.; Lee, C.-R.; Lee, J.-W.; Park, S.-W.; Park, N.-G. 6.5% efficient perovskite quantum-dot-sensitized solar cell. *Nanoscale* **2011**, *3*, 4088–4093. [[CrossRef](#)] [[PubMed](#)]
12. Zhu, Z.; Ma, J.; Wang, Z.; Mu, C.; Fan, Z.; Du, L.; Bai, Y.; Fan, L.; Yan, H.; Phillips, D.L.; et al. Efficiency enhancement of perovskite solar cells through fast electron extraction: The role of graphene quantum dots. *J. Am. Chem. Soc.* **2014**, *136*, 3760–3763. [[CrossRef](#)] [[PubMed](#)]
13. Tang, D.; Liu, J.; Wu, X.; Liu, R.; Han, X.; Han, Y.; Huang, H.; Liu, Y.; Kang, Z. Carbon quantum Dot/NiFe layered double-hydroxide composite as a highly efficient electrocatalyst for water oxidation. *ACS Appl. Mater. Interfaces* **2014**, *6*, 7918–7925. [[CrossRef](#)] [[PubMed](#)]
14. Niu, H.; Yang, X.; Wang, Q.; Jing, X.; Cheng, K.; Zhu, K.; Ye, K.; Wang, G.; Cao, D.; Yan, J. Electrostatic self-assembly of MXene and edge-rich CoAl layered double hydroxide on molecular-scale with superhigh volumetric performances. *J. Energy Chem.* **2019**, *46*, 105–113. [[CrossRef](#)]
15. Xu, Y.; Wang, R.; Zheng, Y.; Zhang, L.; Jiao, T.; Peng, Q.; Liu, Z. Facile preparation of self-assembled Ni/Co phosphates composite spheres with highly efficient HER electrocatalytic performances. *Appl. Surf. Sci.* **2020**, *509*, 145383–145430. [[CrossRef](#)]
16. Jellicoe, T.; Richter, J.M.; Glass, H.F.J.; Tabachnyk, M.; Brady, R.; E Dutton, S.; Rao, A.; Friend, R.H.; Credgington, D.; Greenham, N.C.; et al. Synthesis and optical properties of lead-free cesium tin halide perovskite nanocrystals. *J. Am. Chem. Soc.* **2016**, *138*, 2941–2944. [[CrossRef](#)]
17. Chen, Y.; Zhao, Y. Incorporating quantum dots for high efficiency and stable perovskite photovoltaics. *J. Mater. Chem. A* **2020**, *8*, 25017–25027. [[CrossRef](#)]
18. Stoumpos, C.; Malliakas, C.D.; Peters, J.A.; Liu, Z.; Sebastian, M.; Im, J.; Chasapis, T.C.; Wibowo, A.; Chung, D.Y.; Freeman, A.J.; et al. Crystal growth of the perovskite semiconductor CsPbBr₃: A new material for high-energy radiation detection. *Cryst. Growth Des.* **2013**, *13*, 2722–2727. [[CrossRef](#)]
19. Protesescu, L.; Yakunin, S.; Bodnarchuk, M.; Krieg, F.; Caputo, R.; Hendon, C.; Yang, R.X.; Walsh, A.; Kovalenko, M.V. Nanocrystals of cesium lead halide perovskites (CsPbX₃, X = Cl, Br, and I): Novel optoelectronic materials showing bright emission with wide color gamut. *Nano Lett.* **2015**, *15*, 3692–3696. [[CrossRef](#)]
20. Xiang, X.; Lin, H.; Xu, J.; Cheng, Y.; Wang, C.; Zhang, L.; Wang, Y. CsPb(Br,I)₃ embedded glass: Fabrication, tunable luminescence, improved stability and wide-color gamut LCD application. *Chem. Eng. J.* **2019**, *378*, 122255. [[CrossRef](#)]
21. Aboulaich, A.; Michalska, M.; Schneider, R.; Potdevin, A.; Deschamps, J.; Deloncle, R.; Chadeyron, G.; Mahiou, R. Ce-doped YAG nanophosphor and red emitting CuInS₂/ZnS core/shell quantum dots for warm white light-emitting diode with high color rendering index. *ACS Appl. Mater. Interfaces* **2014**, *6*, 252–258. [[CrossRef](#)]
22. Yang, D.D.; Li, X.M.; Wu, Y.; Wei, C.T.; Qin, Z.Y.; Zhang, C.F.; Sun, Z.G.; Li, Y.L.; Wang, Y.; Zeng, H.B. Surface halogen compensation for robust performance enhancements of CsPbX₃ perovskite quantum dots. *Adv. Opt. Mater.* **2019**, *7*, 1900276. [[CrossRef](#)]
23. Long, Z.; Ren, H.; Sun, J.H.; Ouyang, J.; Na, N. High-throughput and tunable synthesis of colloidal CsPbX₃ perovskite nanocrystals in a heterogeneous system by microwave irradiation. *Chem. Comm.* **2017**, *53*, 9914–9917. [[CrossRef](#)] [[PubMed](#)]
24. Dong, Y.; Tang, X.; Zhang, Z.; Song, J.; Niu, T.; Shan, D.; Zeng, H. Perovskite nanocrystal fluorescence-linked immunosorbent assay methodology for sensitive point-of-care biological test. *Matter* **2020**, *3*, 273–286. [[CrossRef](#)]
25. Shamsi, J.; Urban, A.S.; Imran, M.; De Trizio, L.; Manna, L. Metal halide perovskite nanocrystals: Synthesis, post-synthesis modifications, and their optical properties. *Chem. Rev.* **2019**, *119*, 3296–3348. [[CrossRef](#)]
26. Swarnkar, A.; Chulliyil, R.; Ravi, V.K.; Irfanullah, M.; Chowdhury, A.; Nag, A. Colloidal CsPbBr₃ perovskite nanocrystals: Lu-minescence beyond traditional quantum dots. *Angew. Chem. Int. Ed.* **2015**, *54*, 15424–15428. [[CrossRef](#)]
27. Wu, K.; Liang, G.; Shane, Q.; Ren, Y.; Kong, D.; Lian, T. Ultrafast interfacial electron and hole transfer from CsPbBr₃ perovskite quantum dots. *J. Am. Chem. Soc.* **2015**, *137*, 12792–12795. [[CrossRef](#)] [[PubMed](#)]
28. Wang, H.-C.; Lin, S.-Y.; Tang, A.-C.; Singh, B.P.; Tong, H.-C.; Chen, C.-Y.; Lee, Y.-C.; Tsai, T.-L.; Liu, R.-S. Mesoporous Silica Particles Integrated with All-Inorganic CsPbBr₃ Perovskite Quantum-Dot Nanocomposites (MP-PQDs) with high stability and wide color gamut used for backlight display. *Angew. Chem. Int. Ed.* **2016**, *55*, 7924–7929. [[CrossRef](#)] [[PubMed](#)]
29. Pan, A.; He, B.; Fan, X.; Liu, Z.; Urban, J.J.; Alivisatos, A.P.; He, L.; Liu, Y. Insight into the ligand-mediated synthesis of colloidal CsPbBr₃ perovskite nanocrystals: The role of organic acid, base, and cesium precursors. *Acs Nano* **2016**, *10*, 7943–7954. [[CrossRef](#)]
30. Zhang, X.; Xu, B.; Zhang, J.; Gao, Y.; Zheng, Y.; Wang, K.; Sun, X. All-inorganic perovskite nanocrystals for high-efficiency light emitting diodes: Dual-phase CsPbBr₃-CsPb₂Br₅ composites. *Adv. Funct. Mater.* **2016**, *26*, 4595–4600. [[CrossRef](#)]
31. Zhang, J.; Bai, D.; Jin, Z.; Bian, H.; Wang, K.; Sun, J.; Wang, Q.; Liu, S. 3D-2D-0D interface profiling for record efficiency all-inorganic CsPbBr₃ perovskite solar cells with superior stability. *Adv. Energy Mater.* **2018**, *8*, 1703246–1703255. [[CrossRef](#)]
32. Yang, H.; Yin, W.; Dong, W.; Gao, L.; Tan, C.-H.; Li, W.; Zhang, X.; Zhang, J. Enhancing the light-emitting performance and stability in CsPbBr₃ perovskite quantum dots via simultaneous doping and surface passivation. *J. Mater. Chem. C* **2020**, *8*, 14439–14445. [[CrossRef](#)]
33. Guo, Q.; Yuan, F.L.; Zhang, B.; Zhou, S.J.; Zhang, J.; Bai, Y.M.; Fan, L.Z.; Hayat, T.; Alsaedi, A.; Tan, Z.A. Passivation of the grain boundaries of CH₃NH₃PbI₃ using carbon quantum dots for highly efficient perovskite solar cells with excellent environmental stability. *Nanoscale* **2019**, *11*, 115–124. [[CrossRef](#)]

34. Krieg, F.; Ochsenein, S.T.; Yakunin, S.; Brinck, S.t.; Aellen, P.; Suess, A.; Clerc, B.; Guggisberg, D.; Nazarenko, O.; Shynkarenko, Y.; et al. Colloidal CsPbX₃ (X = Cl, Br, I) nanocrystals 2.0: Zwitterionic capping ligands for improved durability and stability. *ACS Energy Lett.* **2018**, *3*, 641–646. [[CrossRef](#)] [[PubMed](#)]
35. Kojima, A.; Ikegami, M.; Teshima, K.; Miyasaka, T. Highly Luminescent lead bromide perovskite nanoparticles synthesized with porous alumina media. *Chem. Lett.* **2012**, *41*, 397–399. [[CrossRef](#)]
36. Hui, X.; Zhao, R.; Zhang, P.; Li, C.; Wang, C.; Yin, L. Low-Temperature Reduction Strategy Synthesized Si/Ti₃C₂ MXene composite anodes for high-performance li-ion batteries. *Adv. Energy Mater.* **2019**, *9*, 1901065. [[CrossRef](#)]
37. Zhang, X.; Bai, X.; Wu, H.; Zhang, X.; Sun, C.; Zhang, Y.; Zhang, W.; Zheng, W.; Yu, W.W.; Rogach, A.L. Water-assisted size and shape control of CsPbBr₃ perovskite nanocrystals. *Angew. Chem. Int. Ed.* **2018**, *57*, 3337–3342. [[CrossRef](#)]
38. Huang, S.; Li, Z.; Kong, L.; Zhu, N.; Shan, A.; Li, L. Enhancing the stability of CH₃NH₃PbBr₃ quantum dots by embedding in silica spheres derived from tetramethyl orthosilicate in “Waterless” toluene. *J. Am. Chem. Soc.* **2016**, *138*, 5749–5752. [[CrossRef](#)]
39. Raja, S.N.; Bekenstein, Y.; Koc, M.A.; Fischer, S.; Zhang, D.; Lin, L.; Ritchie, R.O.; Yang, P.; Alivisatos, A.P. Encapsulation of perovskite nanocrystals into macroscale polymer matrices: Enhanced stability and polarization. *ACS Appl. Mater. Interfaces* **2016**, *8*, 35523–35533. [[CrossRef](#)]
40. Patil, U.; Fihri, A.; Emwas, A.-H.; Polshettiwar, V. Silicon oxynitrides of KCC-1, SBA-15 and MCM-41 for CO₂ capture with excellent stability and regenerability. *Chem. Sci.* **2012**, *3*, 2224–2229. [[CrossRef](#)]
41. Boutros, M.; Maoui, Z.; Sfihi, H.; Viossat, V.; Gédéon, A.; Launay, F. Effect of the anchorage of Rh(III) ions by imidazoline type ligands on the location of Rh₀ particles within the calcined form of the SBA-15 support. *Microporous Mesoporous Mater.* **2008**, *108*, 247–257. [[CrossRef](#)]
42. Mandache, I.; Parvulescu, V.I.; Popescu, A.; Parvulescu, L.; Banciu, M.D.; Amoros, P.; Beltran, D.; On, D.T.; Kaliaguine, S. Epox-iation of dibenzocycloalkenes on Ti-Ge-MCM-41 and Ti-SBA-15 catalysts. *Microporous Mesoporous Mat.* **2005**, *81*, 115–124. [[CrossRef](#)]
43. Sousa, W.R.D.N.; Oliveira, A.R.; Filho, J.F.C.; Dantas, T.C.M.; Santos, A.G.D.; Caldeira, V.; Luz, G.E. Ciprofloxacin adsorption on ZnO supported on SBA-15. *Water Air Soil Pollut.* **2018**, *229*, 125. [[CrossRef](#)]
44. Colmenares, M.G.; Simon, U.; Schmidt, F.; Dey, S.; Schmidt, J.; Thomas, A.; Gurlo, A. Tailoring of ordered mesoporous silica COK-12: Room temperature synthesis of mesocellular foam and multilamellar vesicles. *Microporous Mesoporous Mater.* **2018**, *267*, 142–149. [[CrossRef](#)]